AIAA SciTech Forum
January 3-7, 2022, San Diego, CA & Virtual
AIAA SCITECH 2022 Forum

10.2514/6.2022-0947

Hypersonic Boundary-Layer Instability on a Highly Cooled Cone. Part II: Schlieren Analysis of Boundary-Layer Disturbances

Laura A. Paquin,* Shaun N. Skinner,† Stuart J. Laurence,‡
University of Maryland, College Park, MD 20742
Ahsan Hameed,§ David Shekhtman,¶ Nick J. Parziale,‖
Stevens Institute of Technology, Hoboken, NJ, 07030
Wesley M. Yu,**and Joanna M. Austin††
California Institute of Technology, Pasadena, CA, 91125

A campaign of hypervelocity experiments was conducted with a blunted 5°-half-angle cone in the T5 shock tunnel. A modified Z-type schlieren setup was utilized to image the boundary-layer with total enthalpies h_0 around 10 MJ/kg and freestream-to-wall temperature ratios T_∞/T_w of approximately 5. Second-mode instabilities and transitional behavior in the boundary layer were identified imaged within the field of view between $x/L = 0.57$ and 0.73. Second-mode wavepackets manifested as alternating dark/light waves beginning right at the wall and permeating up to 30% of the boundary-layer height δ. Spectral analysis of the two lower-Reynolds-number shots demonstrated that these packets could be characterized by peak wavenumbers $315 - 365$ m^{-1} at 10% δ. In the highest-Reynolds-number shot, structures passing out of the boundary layer indicated the beginning of turbulent breakdown. For discrete examples where the onset of these structures was imaged, breakdown appeared to begin at $x/L = 0.66$. A Gabor-filter-based image analysis indicated that spectral content was transferred out of the boundary layer at disturbance Mach numbers 2.75-3.75. A larger range of wavenumbers, $305 - 415$ m^{-1}, populated the near-wall content in this transitional shot, and high-wavenumber content up to 450 m^{-1} was identified outside the boundary layer. It is to be noted that this paper serves as a companion study to that of Ref. [1], which interrogated the same boundary layer with focused-laser differential interferometry (FLDI).

I. Introduction

Thermal conditions undoubtedly affect every aspect of aircraft and spacecraft design. Material selection and thermal protection system (TPS) outfitting must account for the full range of temperatures experienced during a flight envelope as well as the heating profile due to boundary-layer transition over space and time. While many transition studies have indeed characterized boundary-layer instability in hypersonic flow, only

*Graduate Student, Department of Aerospace Engineering, University of Maryland, College Park, MD 20742, AIAA Student Member.
†Postdoctoral Research Associate, Department of Aerospace Engineering, University of Maryland, College Park, MD 20742, AIAA Member.
‡Associate Professor, Department of Aerospace Engineering, University of Maryland, College Park, MD 20742, AIAA Senior Member.
§Graduate Student, Mechanical Engineering, Stevens Institute of Technology, Hoboken, NJ, 07030, Student AIAA Member.
¶Graduate Student, Mechanical Engineering, Stevens Institute of Technology, Hoboken, NJ, 07030, Student AIAA Member.
‖Associate Professor, Mechanical Engineering, Stevens Institute of Technology, Hoboken, NJ, 07030, AIAA Member.
**Graduate Student, Graduate Aerospace Laboraties, California Institute of Technology, Pasadena, CA, 91125, Student AIAA Member.
††Professor of Aerospace, Graduate Aerospace Laboraties, California Institute of Technology, Pasadena, CA, 91125, AIAA Member.

a minority have done so at flight-relevant enthalpies. By creating significantly elevated freestream-to-wall temperature ratios T_∞/T_w, such enthalpies have been shown to alter the behavior of the boundary layer on slender conical models.

Some studies have characterized the effect of such temperatures on boundary-layer disturbances by measuring the spectral growth, or N factor, of instabilities at transition using the e^N method. Alba et al. and Johnson et al. identified an factor of $N = 5.5$ as a predictor of boundary-layer transition in the NASA Langley Mach-6 and the CUBRC LENS tunnels [2, 3]. Because $N = 5.5$ predicted transition reasonably well for experiments at Mach 7 and Mach 10 with enthalpies h_0 = 2-5 MJ/kg, the discrepancy between this value and typical flight transition values (N = 8-11) was attributed to tunnel freestream noise [3]. For a set of experiments at Mach 7-8 and h_0 = 3-8 MJ/kg in JAXA's HIEST facility, however, Gronvall et al. associated $N = 8.0$ with transition on a 7°-half-angle cone. Similarly, Jewell et al. identified N = 9-10 at transition for a 5°-half-angle cone in air and an air/CO_2 mixture at enthalpies h_0 = 8-10 MJ/kg in T5 [4].

Other studies have focused on the connection between Reynolds number and transition. In a wide comparison of transition experiments, Marineau et al. found second-mode instabilities to reach similar spectral amplitudes at the point of transition regardless of enthalpy, but the growth of these disturbances was much more sensitive to the local Reynolds number in high-enthalpy cases than they were in cold-flow facilities [5]. Germain and Hornung, in the first measurement of boundary-layer transition for $h_0 > 3.5$ MJ/kg, demonstrated that increasing enthalpy caused the transition Reynolds number to increase, and this effect was stronger in air than in nitrogen [6]. Adam and Hornung showed that the transition Reynolds number achieved within T5, when calculated with the Eckert reference temperature, matched that measured in the Reentry-F flight test reasonably well [7]. Unfortunately the relationship between h_0 and Re^*_{tr} in the flight test opposed that seen in the experiments of Refs. [6, 7]: a rise in flight h_0 corresponded to a decrease in Re^*_{tr} [7].

A final category of transition studies has explored the structure and appearance of instabilities. While imaging techniques like schlieren offer unique insight into the evolution of boundary-layer disturbances, it is to be noted that such methods become increasingly difficult in high-enthalpy facilities with limited test times and chemiluminescence. Refs. [8] and [9] characterized the structures of instabilities on a 7°-half-angle cone using schlieren and PCB measurements in two different conventional hypersonic tunnels. Casper et al. quantified the intermittency of instabilities and turbulent spots at Mach 5 and 8 for freestream conditions $7 \leq Re \leq 15 \times 10^6 \mathrm{m}^{-1}$ [8]. Kennedy et al. investigated the evolution of second-mode wavepackets at Mach 10 and 14, $2 \leq Re \leq 7 \times 10^6 \mathrm{m}^{-1}$, and $1 \leq h_0 \leq 2$ MJ/kg, showing an initial double-peaked spectrum around the boundary-layer edge which transformed into a single peak as the packet propagated [9]. Laurence et al. conducted a similar analysis at $M \approx 7$, $2 \leq Re \leq 7 \times 10^6 \mathrm{m}^{-1}$, and h_0 = 3 and 12 MJ/kg. Schlieren images showed that, in the high-enthalpy case, the harmonic intensity at the wall surpassed the signal in the rest of the boundary-layer by a factor of 3, and the instabilities exhibited an abnormal disturbance envelope as they moved in space [10]. Although breakdown into turbulence was not observed in these experiments, it is believed that the unique spectral distribution would distinguish the transition to turbulence from that visualized in conventional facilities. Additionally, it is hypothesized that the strong energy confinement near the wall makes these transitional high-enthalpy boundary layers excellent candidates for flow-control systems like porous plates and absorptive materials.

This work expands on the experimental research investigating stability and transition in the T5 reflected-shock tunnel [11, 12, 13, 14, 15]. The study seeks to fill in the gap in knowledge of transitional high-T_∞/T_w boundary layers on slender cones by characterizing the effect on spectral growth, Reynolds-number influence, and structural development of instabilities both prior to and at the point of transition. Schlieren imaging was utilized to image instability development and breakdown along a 5°-half-angle cone in $h_0 \approx 10$ MJ/kg flow.

II. Facility & Setup

All testing was conducted in the T5 reflected shock tunnel at the California Institute of Technology. The facility design and operation are detailed in Ref. [16] and summarized here briefly.

Moving in the downstream direction, the tunnel can be segmented into the following components: secondary reservoir, piston, compression tube (CT), primary diaphragm, shock tube (ST), secondary diaphragm, contoured nozzle, test section, and dump tank. Before a shot, the test section, dump tank, and both tubes are evacuated. Then the ST is filled with air to desired test-gas pressure P_1, and the CT is filled with an

argon/helium mixture to the desired driver pressure P_{CT}. For this campaign, P_{CT} was kept at 14% argon and 86% helium. Finally the secondary reservoir, upstream of the piston, is filled with compressed air to a specified gage pressure P_{2R}, typically around 1200 psi. Once exposed to the pressure in the secondary reservoir, the 120-kg piston travels downstream, adiabatically compressing the driver gas mixture to a desired value P_4. At this point the pressure difference between the driver gas in the CT and the test gas in the ST is high enough to burst the primary stainless steel diaphram. A shock wave travels through the ST at a speed U_s, compressing the test gas until it is reflected at the downstream end of the ST, bursting the secondary mylar diaphragm. Under tailored operation, the test gas is considered stagnant after being additionally compressed and heated from the shock reflection to an ultimate reservoir pressure P_R and temperature T_R. This stagnant flow is then accelerated through the axizymmetric nozzle to a Mach number of approximately 5.5, and hypervelocity flow is established for about 1 ms in the test section.

Table 1 lists the relevant reservoir and freestream conditions for the tests analyzed below: Shots 2958, 2959 and 2963. The total enthalpy and reservoir conditions were calculated using Cantera and the Shock & Detonation Toolbox [17, 18], and the freestream conditions were generated using University of Minnesota's Nozzle Code, documented in Refs. [19, 20, 21, 22].

Table 1. Shot Conditions

Shot	Reservoir			Freestream						
	P_0 (MPa)	h_0 (MJ/kg)	T_0 (K)	U_∞ (m/s)	P_∞ (kPa)	T_∞ (K)	Re_∞ ($\times 10^6$ m^{-1})	u_p (m/s)	M_∞ –	T_∞/T_w –
2958	58.3	10.22	6289	4045	35.9	1607	5.30	3017	4.99	5.4
2959	57.8	9.76	6099	3973	34.7	1524	5.51	2990	5.04	5.2
2963	60.6	9.30	5915	3902	35.4	1438	6.10	2991	5.10	4.9

Total enthalpies h_0 of approximately 10 MJ/kg were established for all shots, resulting in freestream-to-wall temperature ratios T_∞/T_w of roughly 5. As discussed in the following sections, Shots 2958 and 2959 exhibit very similar boundary-layer behavior: laminar with strong second-mode content. Shot 2963, with the highest unit Reynolds number $Re_\infty = 6.10 \times 10^6$ m^{-1}, demonstrates the beginning of transition to turbulence. The propagation speeds u_p represent the average speed of wavepackets in each run. An average boundary-layer height of $\delta = 1.2$ mm was calculated from the images for all three shots.

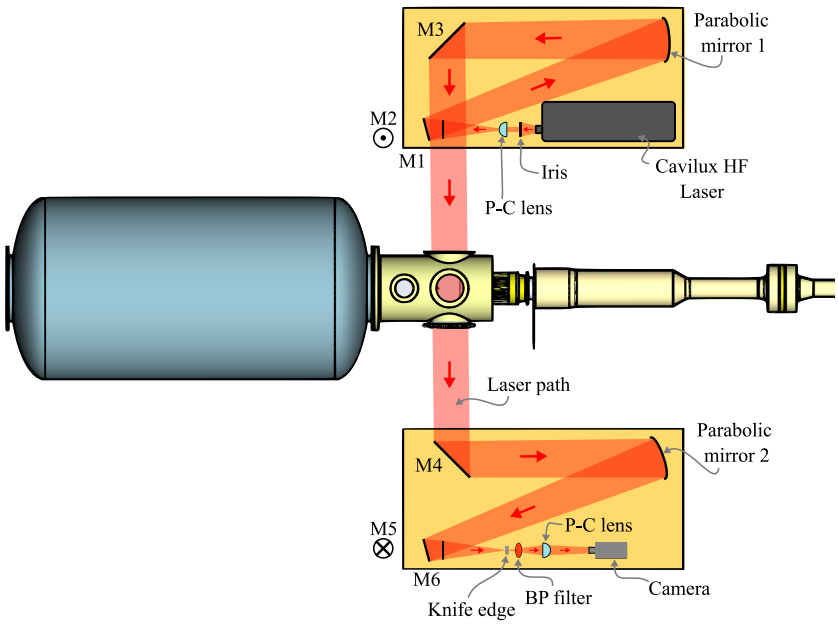

Figure 1. Schematic of schlieren setup

Fig. 1 depicts a simplified schematic of the schlieren setup. As shown on the top (port) side, the light

from the Cavilux HF laser unit was first sent through an adjustable iris diaphragm and then expanded through a plano-convex (P-C) lens. The beam was collimated by a parabolic mirror and directed by a few planar mirrors (M1-M3) through the test section. On the starboard side, the beam was again directed to the level of the camera with a few planar mirrors (M4-M5) . A parabolic mirror focused the beam back down to a point, where the knife edge was inserted. Finally, the beam passed through a bandpass (BP) filter, which prohibited the chemiluminescene from obscuring the signal, and then a long-focal-length plano-convex lens, which provided a pixel/mm scale of 8.7. All imaging was performed with a Phantom v2640 camera at a frame rate of 160 kHz.

The model was a 5°-half-angle cone, 99 cm in length, with a 2-mm nose radius. The field of view was between $x = 57$ and 73 cm along the cone surface, or $0.57 \leq x/L \leq 0.73$.

III. Results

A. Boundary-layer and exterior structures

Fig. 2 shows a series of reference-subtracted schlieren images of the boundary layer from Shots 2958, 2959, and 2963. An erroneous gamma correction caused the image signal in Shot 2958 to have less than half the dynamic range of that from the other shots, and the corrected images thus appear more grainy. Also, some optical warping caused the wall to appear non-flat in this shot.

Boundary-layer height, δ, was measured with a Sobel-filter-based technique, discussed in Ref. [23]. As mentioned in Section II, the average value $\delta = 1.2$ mm was found for all three shots. A wavelet transform was employed to identify the presence of second-mode wavepacket in schlieren images, as discussed in Refs. [8, 23, 24, 25]. A method using cross-correlation of identified second-mode regions in sequential images was used to calculate the average propagation speeds u_p listed in Table 1.

In Shots 2958 and 2959, second-mode wavepackets are especially visible right at the wall, where alternating dark/light waves appear. The example from Shot 2958 in Fig. 2(a) shows various wavepackets entering and leaving the field of view. One wave structure starting at $x = 632$ mm appears to sink into the boundary-layer, nearly diminishing at $x = 660$ mm by $t = 0.169$ ms while another packet starting at $x = 660$ mm grows more prominent as it moves downstream. In Fig. 2(b), one packet moves steadily from $x = 641$ mm to $x = 708$ mm, and the band of light/dark spots grows taller in the boundary layer, demonstrating pointed peaks by $t = 0.281$ ms.

The schlieren sequence in Fig. 2(c) exhibits the transitional state of the boundary layer in Shot 2963. A curved structure arcs from the bottom to the top of the boundary layer at $x = 683$ mm in the first image. Moving downstream, this structure grows into two noticeable streaks that pass out of the boundary layer at $t = 0.081$ ms, sending small disturbances downstream. From then on, turbulent breakdown occurs in the region $x \geq 677$ mm, where the boundary layer grows in height and Mach waves radiate into the freestream. As can be seen, this transitional structure expands as it propagates downstream unlike the wavepackets in Figs. 2(a) and 2(b), which can be easily traced with u_p.

To quantify the trends seen in Fig. 2, the angles of structures inside and outside the boundary layer were computed. For second-mode wavepackets clearly confined within boundary layer, rows of harmonic content were cross-correlated with one another. The structure angle θ at each height y/δ was calculated using the peak displacement Δx and the distance between rows Δy such that $\theta = \tan^{-1}(\Delta y/\Delta x)$. Calculation was stopped when rows exhibited low intensity in the bandwith $k = 2 - 3.5\delta$ or when correlated pairs of rows failed to meet a minimum correlation magnitude. The series of n data points from each image was then fitted with a polynomial of order $n-1$. Fig. 3 shows the results for the wavepacket series imaged in Fig. 2(b). As can be shown, the wave persists only in the region $y/\delta \leq 0.2$ in the first two images but expands to 30% δ by $x = 670$ mm. The structure angle right at the wall θ_{wall} decreases as the packet moves from $x = 641$ mm to 670 mm, indicating that the waves incline more toward the wall in

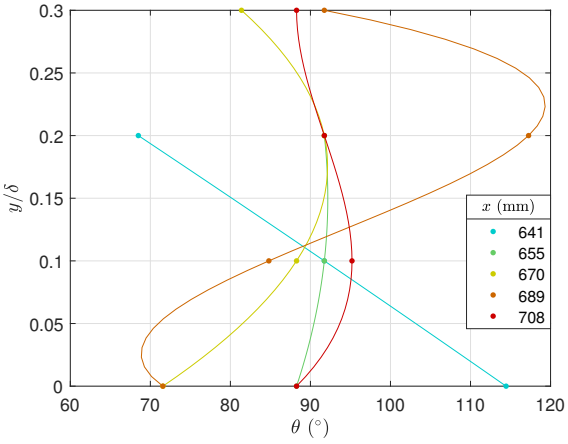

Figure 3. Orientation of waves as a function of wall-normal distance

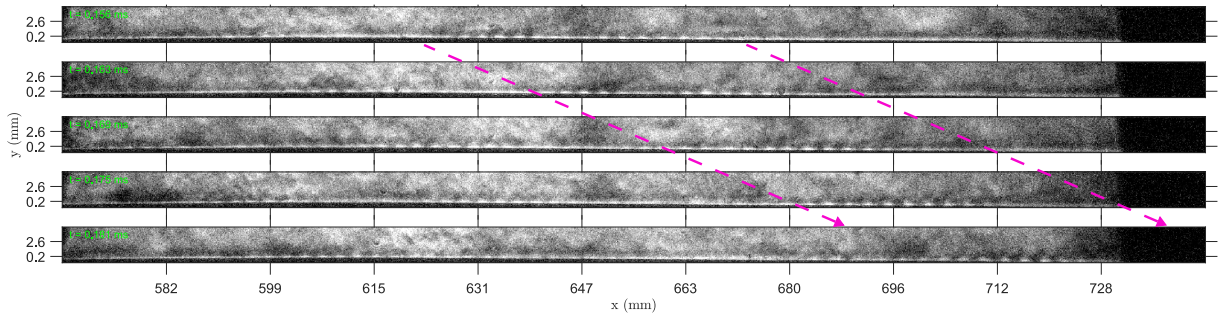

(a) Shot 2958

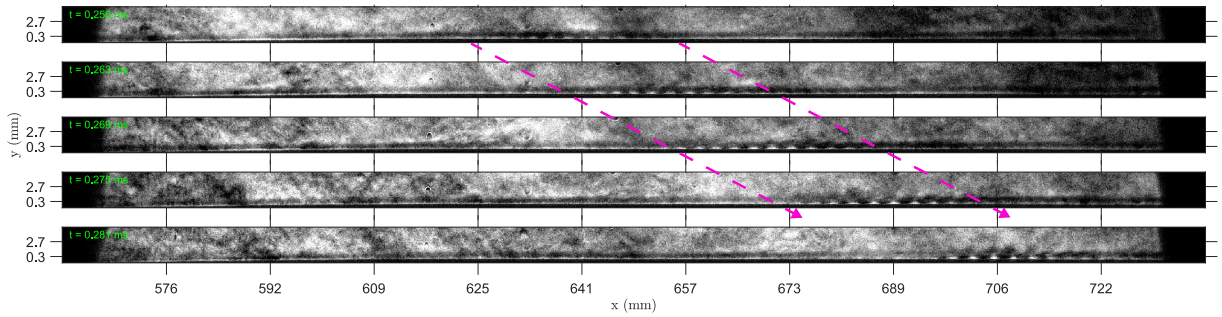

(b) Shot 2959

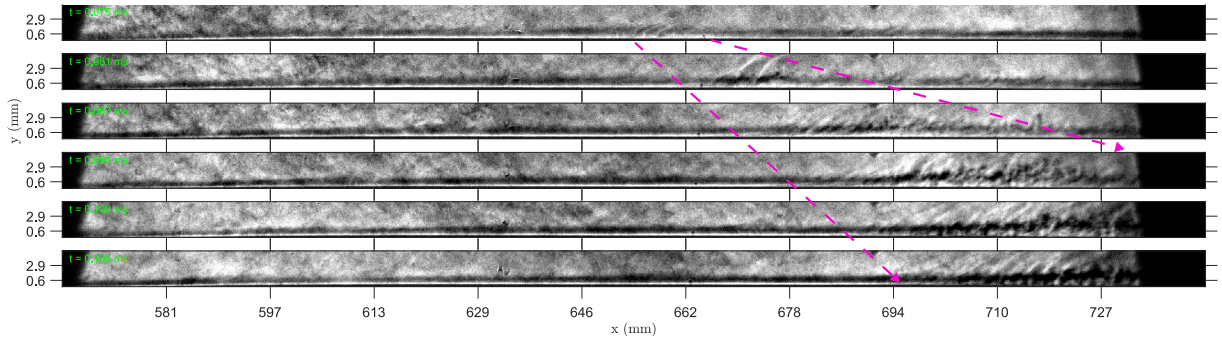

(c) Shot 2963

Figure 2. Series of schlieren images from each shot with regions of interest marked

this region. Then for $x = 689 - 708$ mm, θ_{wall} rises back up,
reaching 88° at $t = 0.281$ ms, where the wavepacket exhibits a largely vertical profile for $y = 0 - 0.3\delta$.

For structures observed just outside δ, a new method was developed to characterize the unique nature of these features which, as shown at $t = 0.087$ ms in Fig. 2(c), often appear as a rippling in the boundary layer and nearby freestream. Methods based on Gabor filtering have been implemented to extract features within the field of texture analysis [26]. For this reason, Gabor filtering was utilized to quantify the orientation of structures extending out of the boundary layer in Run 2963. Segments of images with rippled texture were identified, and a bank of Gabor filters oriented $10° \leq \theta \leq 80°$ was used to interrogate overlapping windows within each segment. The magnitude of each filter response was calculated using a sum-of-squares routine, and angles which generated local maxima in the response magnitude were identified as the local structure angle. Resulting structure angles for the five images $t = 0.810 - 0.106$ ms in Fig. 2(c) are drawn on the segments in Fig. 4.

Segments of the vector fields shown in Fig. 4 were averaged to provide mean profiles of the exterior feature as it moves downstream. The averaged profiles are displayed in Fig. 5, and linear fits, shown as dashed lines, assisted in calculating the Mach angle of the features. The corresponding relative Mach number increases from $M_{rel} = 1.1$ at $x = 674$ mm to $M_{rel} = 2.1$ at $x = 715$ mm, where $M_{rel} = M_e - M_{dist}$. This indicates that, with an expected edge Mach number $M_e = 4.85$, the disturbance Mach number M_{dist} (in a

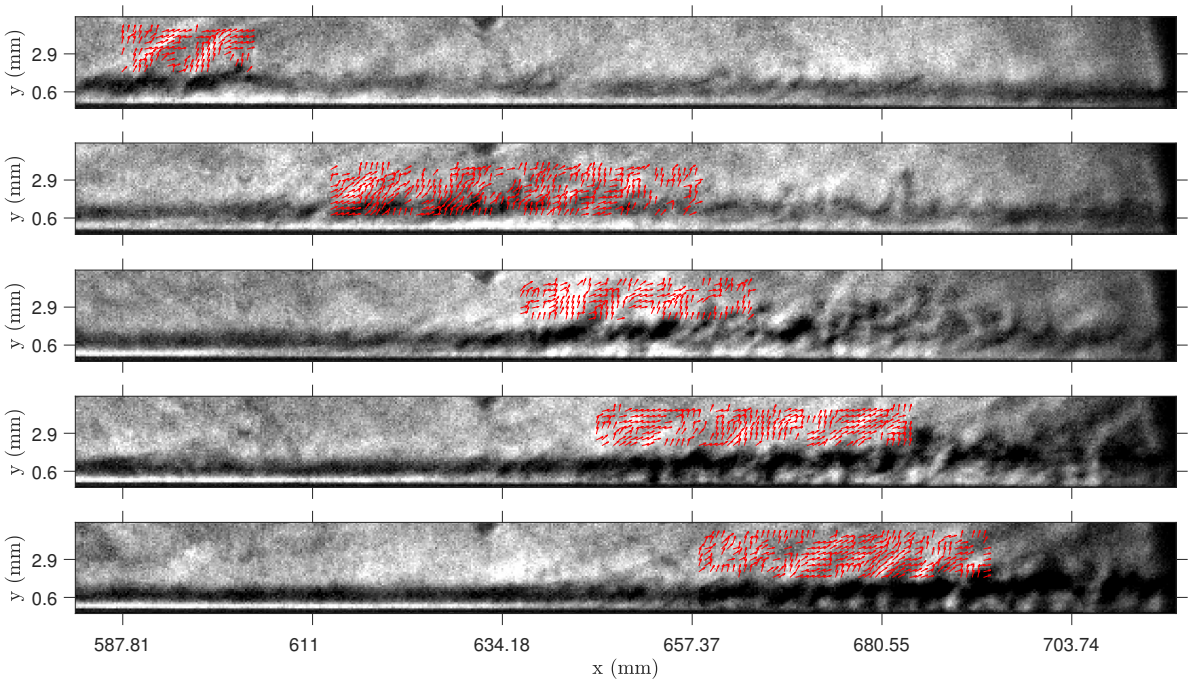

Figure 4. Feature angles computed by Gabor filtering

lab-stationary frame) decreases from 3.75 to 2.75.

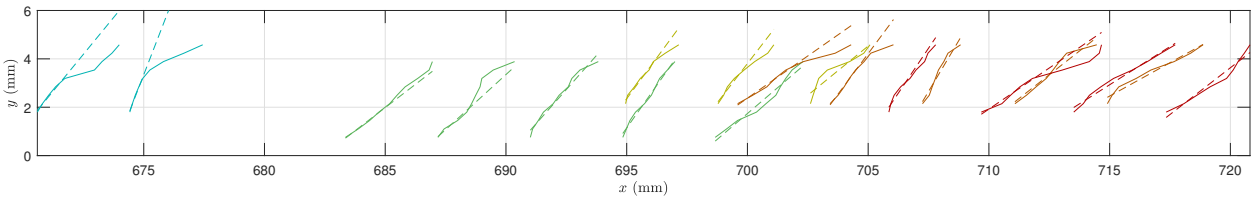

Figure 5. Averaged feature angles and associated Mach lines

B. Spectral content

Apart from their size and orientation, instabilities were also characterized by their spectral content. Wavenumber spectra were calculated for pixel signals at approximately $10\%\delta$ for a central bin $627 < x < 680$ mm within each image. A Blackman window was applied to the bin intensity profile before the power-spectral density (PSD) was computed over the wavenumber domain k. Fig. 6 shows the resulting heat map generated by aggregating all image spectra from the duration of each shot. Figs. 6(a) and 6(b) demonstrate the laminar state of the boundary layer in Shots 2958 and 2959, which both experience only short bursts of second-mode content around $k = 350$ m^{-1}. The heat map in Fig. 6(c) exhibits the transitional state of this boundary layer, which experiences broadband turbulent content for $t = 0.15 - 0.27$ ms and $t = 0.88 - 0.95$ ms in addition to short bursts of second-mode activity centered around $k = 370$ m^{-1}.

These time-resolved maps were instrumental in identifying images with wavepackets and other notable features. For example, the schlieren sequence in Fig. 2(a) corresponds to the multi-lobed bright spot at $t = 0.16$ ms in Fig. 6(a), and the series shown in Fig. 2(b) corresponds to the strong burst at $t = 0.27$ ms in 6(b). While strong second-mode wavepackets did not persist in Shot 2963 as much as they did in 2958 and 2959, the unique exterior structures often followed fleeting moments of second-mode content. For example, the streaks identified in Figs. 2(c) and 4 followed the $k = 280$ m^{-1} burst at $t = 0.62$ ms in Fig. 6(c). Similarly, the features analyzed later in this section follow the $k = 370$ m^{-1} burst at $t = 0.59$ ms.

To investigate the evolution of energy within the boundary layer as instabilities move downstream,

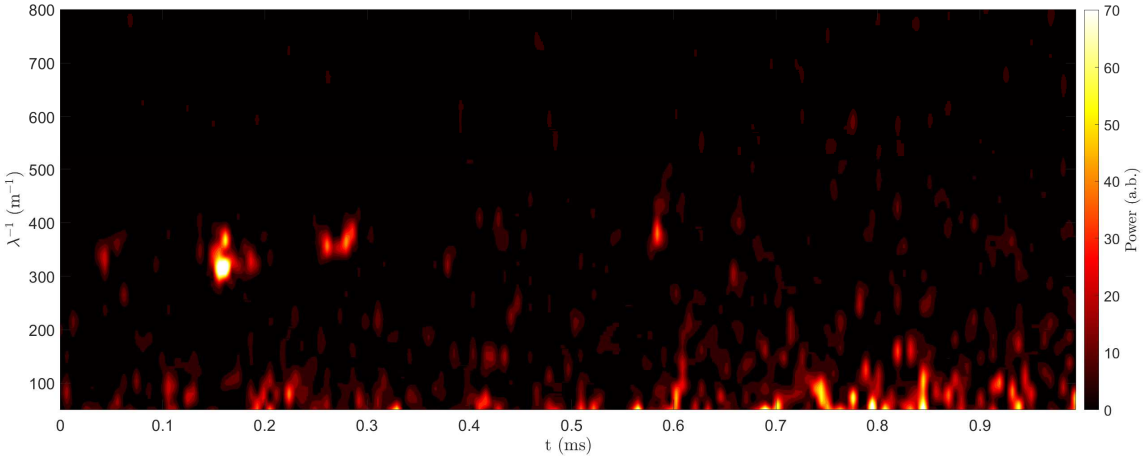

(a) Run 2958 spectra over time

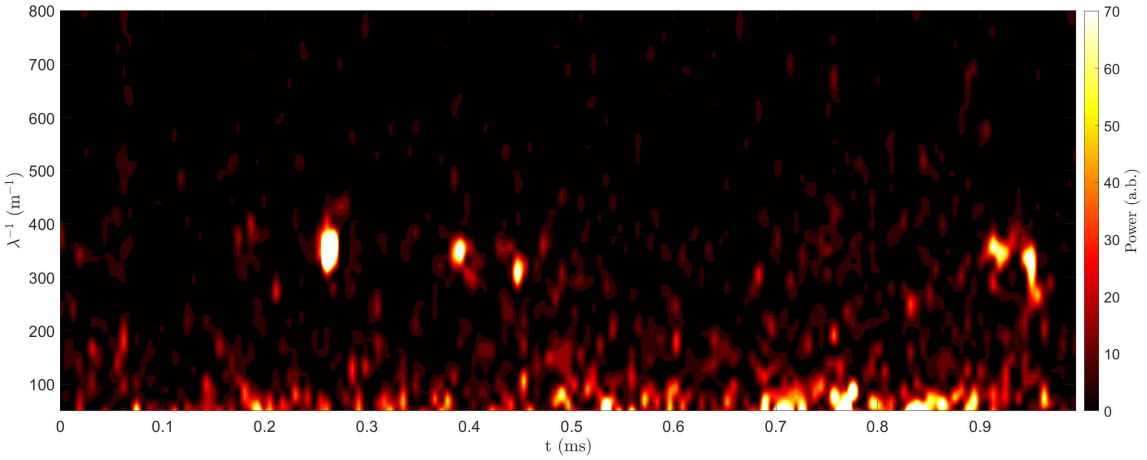

(b) Run 2959 spectra over time

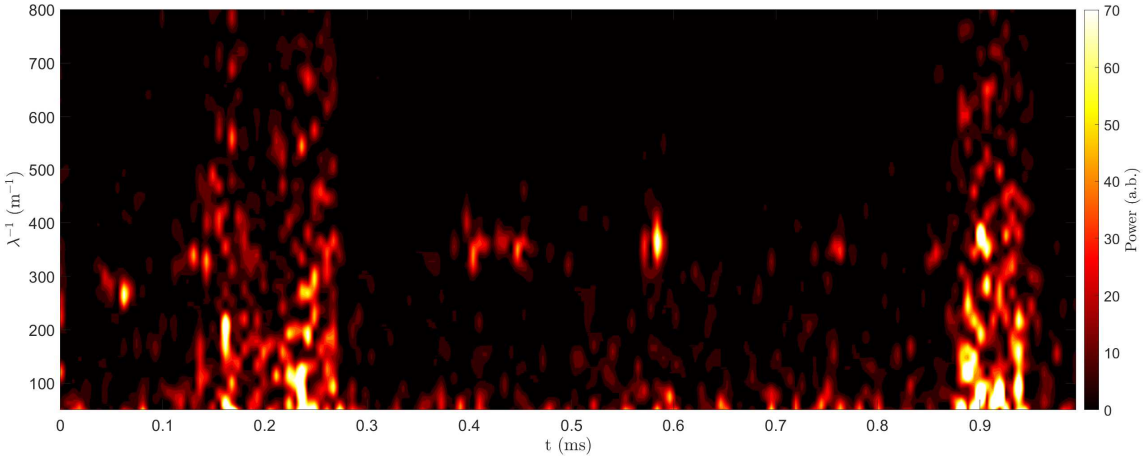

(c) Run 2963 spectra over time

Figure 6. Wavenumber spectra throughout run durations

wavenumber spectra were also computed at various wall-normal heights. Regions of notable second-mode activity were identified and tracked using the mean propagation speeds u_p presented in Table 1. In the schlieren series of Figs. 7-9, the bounds of these regions are marked, and the resulting spectra are displayed.

Fig. 7 provides insight into the multi-lobed second-mode burst at $t = 0.16$ ms in Shot 2958, discussed previously in Figs. 2(a) and 6(a). It is important to note that, due to the image warping, the y/δ values are not exact for this shot. One strong peak around $k = 365$ m^{-1} corresponds to the content right at the wall within the marked region in the first frame of Fig. 7(a). As the wave progresses downstream, it splits into two wave structures visible within the bounds at $t = 0.156 - 0.163$ ms, and the content in Fig. 7(b) bifurcates into two peaks, $k = 315$ and 365 m^{-1}. By $t = 0.163$ ms the power of the higher-k peak drops to less than half that of the lower-k peak for 10-20% δ, and from then on, only one wavepacket persists within the bounds, growing taller as it moves downstream. The higher-k peak completely diminishes as the lower-k peak doubles in size at $t = 0.169$ ms. This peak persists, distributing more energy higher into the boundary layer. It is to be noted that the z limits on only the fourth and fifth plots were increased to make the growth of the low-k peak visible without obscuring the lower-power split content in the previous plots. Ultimately, this analysis shows the apparent splitting of second-mode content leading to the attenuation of high-k content amid growth and spatial redistribution of lower-k content.

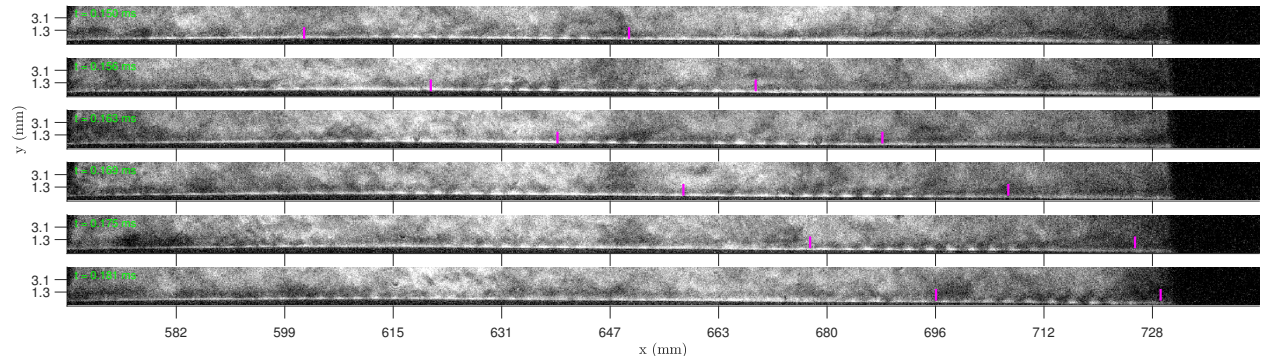

(a) Image series from Run 2958

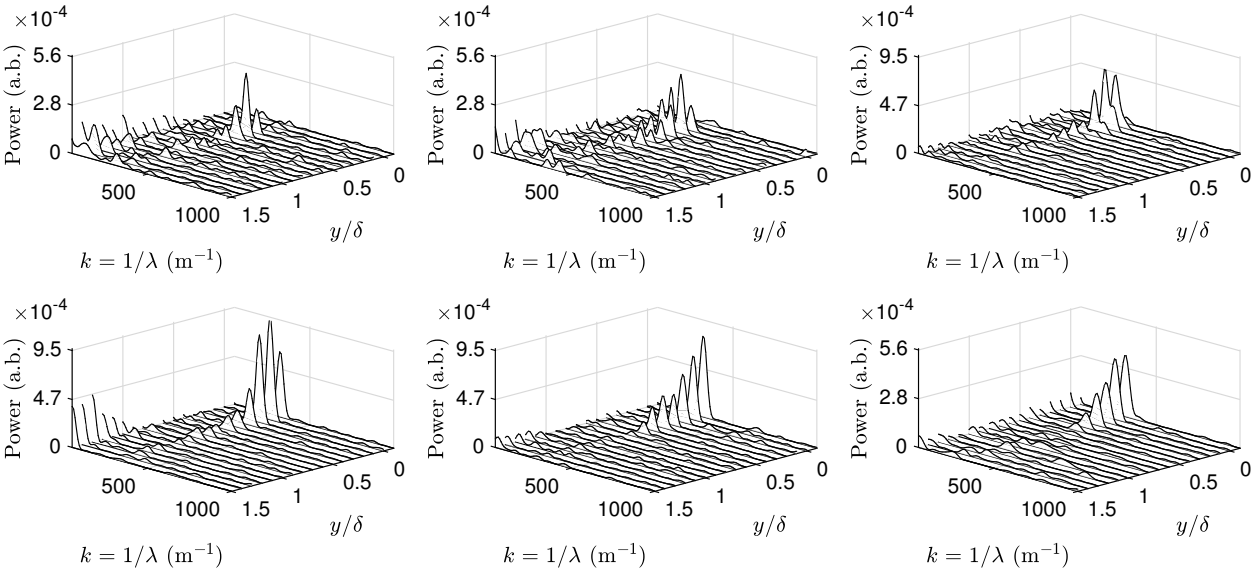

(b) Wall-normal spectral content. Top row (left → right) corresponds to frames $t = 0.150 \rightarrow 0.163$ ms. Bottom row (left → right) corresponds to frames $t = 0.169 \rightarrow 0.181$ ms.

Figure 7. Wall-normal wavenumber spectra for Run 2958

Fig. 8 expands the analysis of the content at $t = 0.27$ ms in Shot 2959, also discussed previously in Figs. 2(b) and 6(b). The second-mode content in these images demonstrates a mugh higher signal-to-noise ratio, producing PSD powers an order of magnitude higher than that in other two shots. The content at the

wall in the first image results in a $k = 355$ m^{-1} peak at at 10% δ. This 10%-δ peak remains the maximum throughout the series, nearly quadrupling in power at $t = 0.269$ ms and then decreasing by $t = 0.281$ ms. As the wavepacket propagates, the peak wavenumber shifts gradually from 355 m^{-1} to 335 m^{-1}, and energy is distributed slightly higher in the boundary layer. For example, at $t = 0.269$ ms the peak power at $y/\delta = 0.3$ sits at 10% of the maximum $y/\delta = 0.1$ peak but rises to 30% of the maximum at $t = 0.281$ ms. Unlike the example from Shot 2958, this series does not exemplify the coexistence of multiple modes of harmonic content; rather, it demonstrates the growth and spatial redistribution of a strong second-mode disturbance.

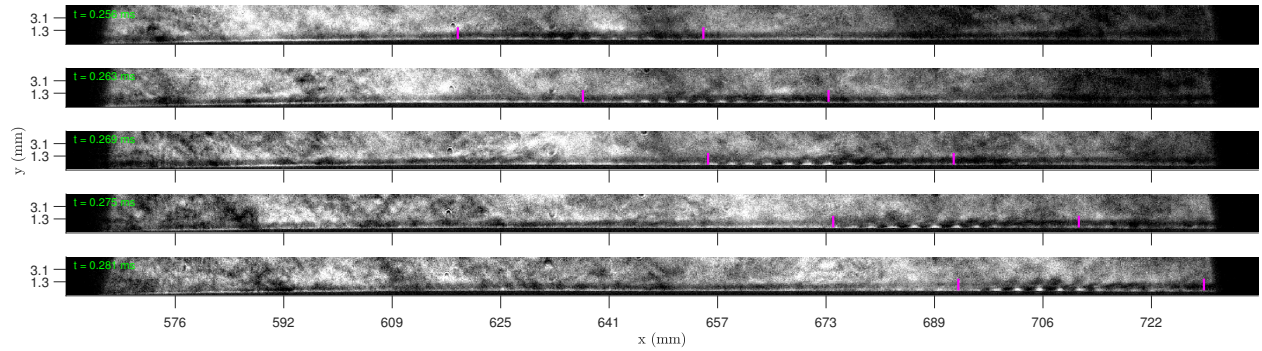

(a) Image series from Run 2959

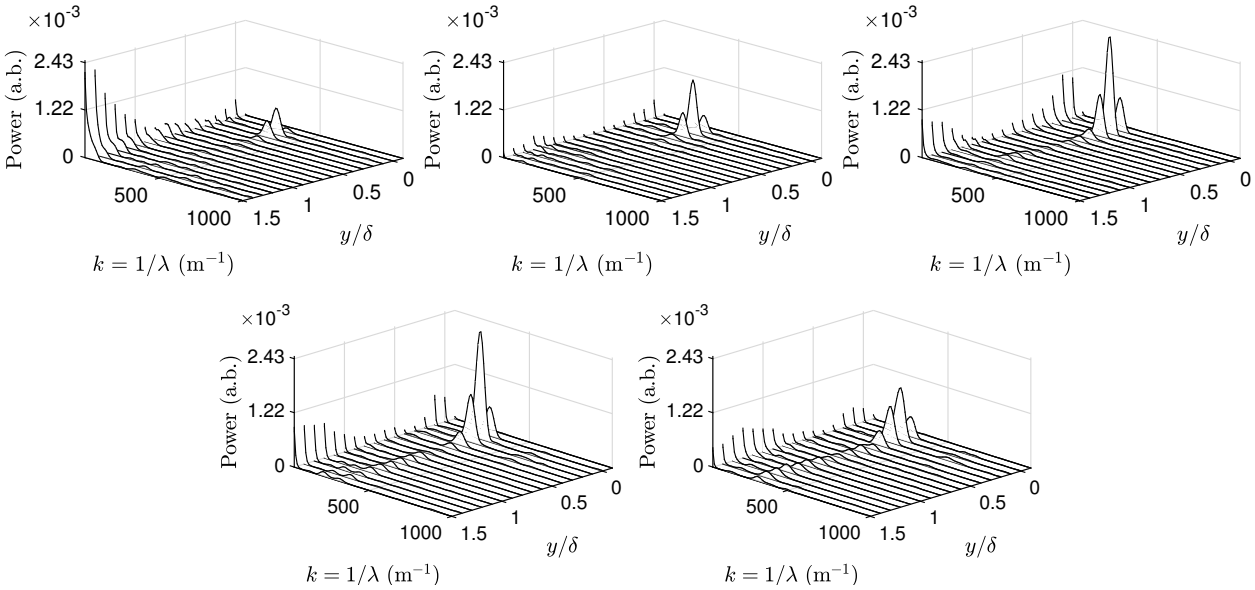

(b) Wall-normal spectral content. Top row (left → right) corresponds to frames $t = 0.256 \rightarrow 0.269$ ms. Bottom row (left → right) corresponds to frames $t = 0.275 \rightarrow 0.281$ ms.

Figure 8. Wall-normal wavenumber spectra for Run 2959

Finally, Fig. 9 explores the evolution of wavenumber content for the most noticeable second-mode burst from Shot 2963, seen at $t = 0.59$ ms in Fig. 6(c). Similar to the other shots, the series starts with a band of alternating dark/light spots right at the wall which becomes most prominent at $x = 640$ mm at $t = 0.588$ ms. Two small peaks, $k = 305$ and 415 m^{-1}, correspond to the subtle second-mode band in the first image. By $t = 0.588$ ms the peaks have combined and tripled in power, generating a strong 360 m^{-1} peak at 10% δ and a secondary split peak at 20% δ.

The subsequent development distinguishes this transitional shot from the others, exhibiting a mechanism by which energy is transferred out of the boundary layer as the breakdown to turbulence commences. A curved feature extends out of the marked region at $t = 0.594$ ms, decreasing the power of the 10%-δ peak. In the following frame, a periodic structure extends outside the boundary layer at the lefthand side of the marked region, creating a second periodic layer on top of the wavepacket confined within δ. The spectra reflects this observation; high-k content around 440-450 m^{-1} is introduced over $y/\delta = 1 - 1.4$, exceeding the

power of the 10%-δ peak which has lowered to 305 m^{-1}. Moving downstream, more structures extend out of the boundary layer, creating the rippling appearance of Mach waves radiating into the freestream, discussed earlier. Even amid this apparent energy transfer out of the boundary layer, the strongest peak of the series at 330 m^{-1} emerges at $t = 0.606$ ms, distributing content up to $y/\delta = 0.4$. Then, high-k content again seems to rise out of the boundary layer; the peak in the lower half of δ shrinks, and content at 390-450 m^{-1} arises over $y/\delta = 1-1.4$. The orientation of the structures likely represents the speed at which such content travels out of the boundary layer. The disturbance orientation in Fig. 5 suggests that radiated content slows down as it propagates downstream.

The large range of harmonic content, $305 \leq k \leq 450$ m^{-1}, in this example indicates that the boundary layer is on the brink of turbulent breakdown. The apparent back-and-forth transfer of spectral content between the boundary layer and the nearby freestream was associated with other features in this run, such as the exterior structures in Fig. 2(c), and is thus considered representative of its spectral behavior. While the example from Shot 2958 demonstrates the attenuation of high-k content, this shot seems to show how such content it is transferred outside δ. It is to be noted that based on two discrete examples, seen in Figs. 2(c) and 8(a), the boundary layer in Shot 2963 appears to begin breakdown around $x/L = 0.66$; however, transition in the shot was highly intermittent. During the broadband bursts depicted in Fig. 6(c), turbulent spots passed through the entirety of the field of view, but at other times, the flow was entirely laminar.

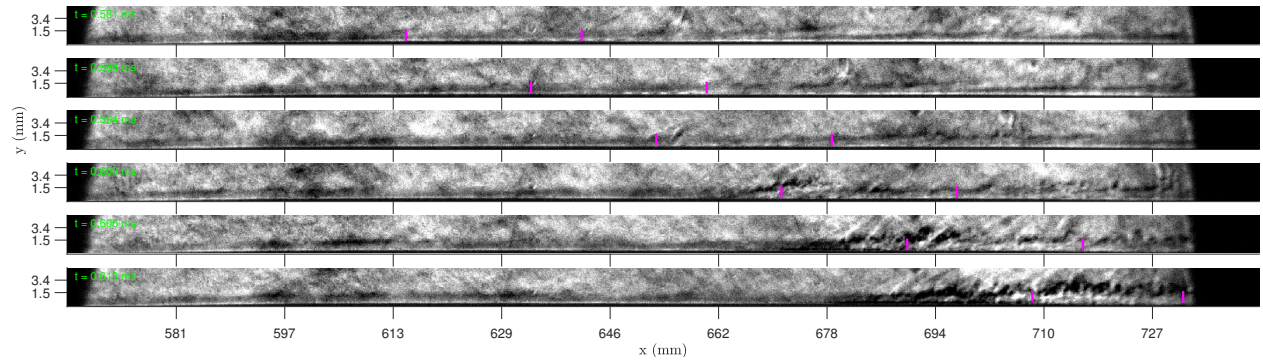

(a) Image series from Run 2963

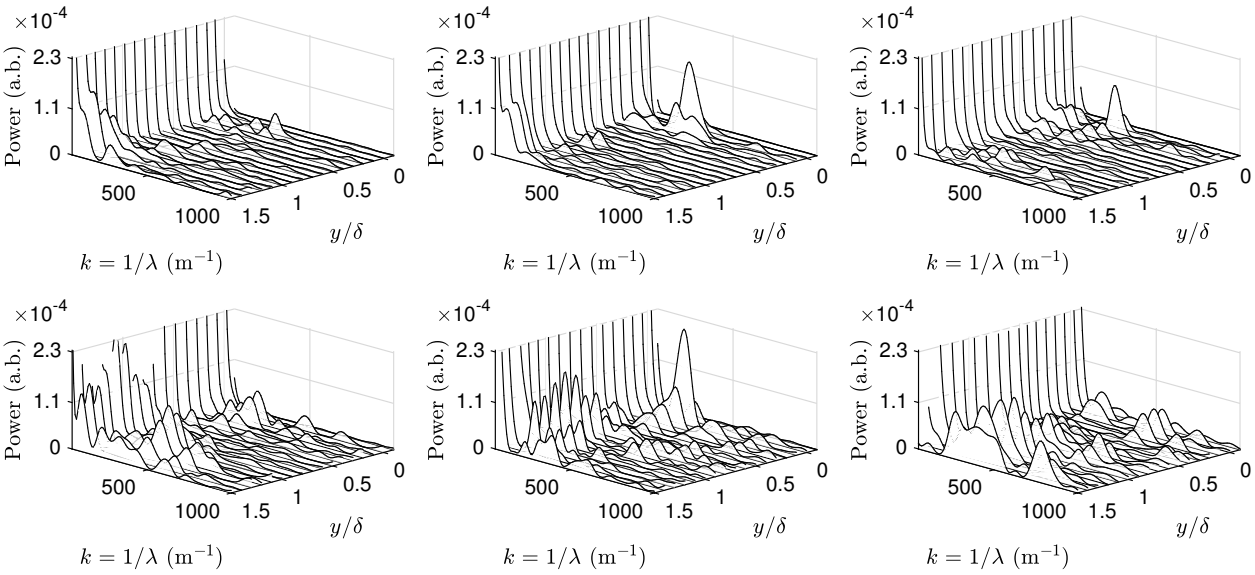

(b) Wall-normal spectral content. Top row (left → right) corresponds to frames $t = 0.581 \rightarrow 0.594$ ms. Bottom row (left → right) corresponds to frames $t = 0.600 \rightarrow 0.613$ ms.

Figure 9. Wall-normal wavenumber spectra for Run 2963.

To visualize some of the spectral content in frequency space in addition to the wavenumber domain, wavenumber spectra were multiplied by mean propagation speed such that $f = u_p \times k$. Fig. 10 compares the PSD of the content at 10% δ in the region $627 < x < 680$ mm from each shot. The spectra were each averaged over a 0.3-ms period where second-mode content was observed but turbulent breakdown was not present. As can be seen, the peak power in Shot 2959 at $f = 1060$ kHz exceeds that of the other two shots by a factor of 2, indicating a much stronger signal-to-noise ratio in this case. The 1060-kHz peak corresponds to a wavenumber $k = 355$ m^{-1}, which could be expected from Fig. 6(b). The peak frequency for Shot 2963 at $f = 1070$ kHz corresponds to $k = 360$ m^{-1}, the strong peak seen in the wall-normal spectra of Fig. 9(b). Most unique, Shot 2958 experiences a split peak with notable energy at 1070 kHz and slightly higher power at 965 kHz. These peaks correspond to wavenumbers $k = 320$ m^{-1} and 355 m^{-1}, similar to those observed in the multi-lobed bright spot at $t = 0.16$ ms in Fig. 6(a) and the wall-normal spectra for $t = 0.156$ ms in Fig. 7(b). The peaks at 1060 kHz in Shot 2959 and 1070 kHz in Shots 2963 and 2958 all correspond to 43% u_p/δ, and the 965-kHz peak represents 38% u_p/δ.

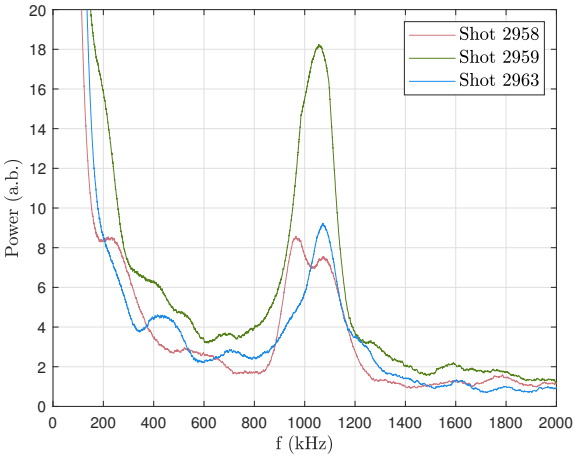

Figure 10. Averaged frequency spectra

IV. Conclusion

Boundary-layer instability and breakdown was visualized along a slender cone at high-enthalpy conditions. Reservoir pressures of $P_R = 58$-61 MPa and specific total enthalpies of $h_0 = 9.3$-10.22 MJ/kg were found to produce strong second-mode content as well as intermittent turbulence. Shots 2958 and 2959 exhibit second-mode instabilities with the highest PSD content at 10% δ; however, the structure angle and wavenumber spatial distribution evolve as these instabilities move downstream. In Shot 2958, distinct wave structures populate the frame $570 \leq x \leq 730$ mm, and a high-wavenumber peak attenuates as a lower-wavenumber peak grows in strength. Waves in Shot 2959 tend to incline more toward the wall in the beginning of their development and then revert to a vertical profile once expanded to 30% δ. In this shot, an extremely strong second-mode peak persists, shifting from $k = 355$ to 335 m^{-1}. Shot 2963, the highest Re_∞, demonstrates intermittent turbulent bursts, indicating the beginning of turbulent breakdown in the range $0.57 \leq x/L \leq 0.73$. Structures extending out of the boundary layer often follow fleeting bursts of second-mode content, starting as individual disturbances and evolving into a series of Mach waves which "ripple" through the boundary layer and nearby freestream. The combination of a Gabor-filtering technique and spectral analysis suggests that these waves provide a mechanism by which high-k content is transferred out of the boundary at disturbance Mach numbers $M_{dist} = 2.75 - 3.75$. Wall-normal spectra depict spectral peaks alternating between lower-k near-wall content and higher-k content over $y/\delta = 1 - 1.4$. In instances where the onset of these structures was observed, breakdown appeared to begin at $x/L = 0.66$. The quantity 43% u_p/δ was found to predict second-mode frequency peaks in all cases, with Shot 2958 (lowest Re_∞, highest T_∞/T_w) also demonstrating a peak at $f = 38\% u_p/\delta$.

Acknowledgments

This work was supported by AFOSR grant FA9550-18-1-040, under program manager Sarah Popkin. The authors would like to acknowledge the vast knowledge of Bahram Valiferdowsi and Noel Esparza-Duran in operating the tunnel. Laura Paquin would also like to acknowledge financial support from the Metropolitan Washington Chapter of the ARCS Foundation.

References

[1] Hameed, A., Shekhtman, D., Parziale, N. J., Paquin, L. A., Skinner, S. N., Laurence, S. J., Yu, W. M., and Austin, J. M., "Hypersonic Boundary-Layer Instability on a Highly Cooled Cone. Part I: Q-FLDI

Measurement and Instability Calculations," *AIAA Scitech 2022 Forum*, 2022, p. xxxx, Abstract submitted.

[2] Alba, C. R., Johnson, H. B., Bartkowicz, M. D., Candler, G. V., and Berger, K. T., "Boundary-layer stability calculations for the HIFiRE-1 transition experiment," *Journal of Spacecraft and Rockets*, Vol. 45, No. 6, 2008, pp. 1125–1133.

[3] Johnson, H., Alba, C., Candler, G., MacLean, M., Wadhams, T., and Holden, M., "Boundary-layer stability analysis of the hypersonic international flight research transition experiments," *Journal of Spacecraft and Rockets*, Vol. 45, No. 2, 2008, pp. 228–236.

[4] Jewell, J., Wagnild, R., Leyva, I., Candler, G., and Shepherd, J., "Transition within a hypervelocity boundary layer on a 5-degree half-angle cone in air/CO2 mixtures," *51st AIAA Aerospace Sciences Meeting Including the New Horizons Forum and Aerospace Exposition*, 2013, p. 523.

[5] Marineau, E. C., Grossir, G., Wagner, A., Leinemann, M., Radespiel, R., Tanno, H., Chynoweth, B. C., Schneider, S. P., Wagnild, R. M., and Casper, K. M., "Analysis of Second-Mode Amplitudes on Sharp Cones in Hypersonic Wind Tunnels," *Journal of Spacecraft and Rockets*, Vol. 56, No. 2, 2019, pp. 307–318.

[6] Germain, P. and Hornung, H., "Transition on a slender cone in hypervelocity flow," *Experiments in Fluids*, Vol. 22, No. 3, 1997, pp. 183–190.

[7] Adam, P. H. and Hornung, H. G., "Enthalpy effects on hypervelocity boundary-layer transition: ground test and flight data," *Journal of Spacecraft and Rockets*, Vol. 34, No. 5, 1997, pp. 614–619.

[8] Casper, K. M., Beresh, S. J., Henfling, J., Spillers, R., and Pruett, B., "Transition Statistics Measured on a 7-Degree Hypersonic Cone for Turbulent Spot Modeling," *52nd Aerospace Sciences Meeting*, 2014, p. 0427.

[9] Kennedy, R. E., Laurence, S. J., Smith, M. S., and Marineau, E. C., "Hypersonic Boundary-Layer Transition Features from High-Speed Schlieren Images," *55th AIAA Aerospace Sciences Meeting*, 2017, p. 1683.

[10] Laurence, S., Wagner, A., and Hannemann, K., "Experimental study of second-mode instability growth and breakdown in a hypersonic boundary layer using high-speed schlieren visualization," *Journal of Fluid Mechanics*, Vol. 797, No. 3, 2016, pp. 471–503.

[11] Parziale, N., Shepherd, J., and Hornung, H., "Differential interferometric measurement of instability in a hypervelocity boundary layer," *AIAA journal*, Vol. 51, No. 3, 2013, pp. 750–754.

[12] Parziale, N., Shepherd, J., and Hornung, H., "Free-stream density perturbations in a reflected-shock tunnel," *Experiments in Fluids*, Vol. 55, No. 2, 2014, pp. 1–10.

[13] Parziale, N., Shepherd, J., and Hornung, H., "Observations of hypervelocity boundary-layer instability," *Journal of Fluid Mechanics*, Vol. 781, 2015, pp. 87–112.

[14] Jewell, J. S., Leyva, I. A., and Shepherd, J. E., "Turbulent spots in hypervelocity flow," *Experiments in Fluids*, Vol. 58, No. 4, 2017, pp. 32.

[15] Jewell, J., Leyva, I., Parziale, N. J., and Shepherd, J. E., "Effect of gas injection on transition in hypervelocity boundary layers," *28th International Symposium on Shock Waves*, Springer, 2012, pp. 735–740.

[16] Hornung, H., "Performance data ofthe New Free-Piston Shock Tunnel at GALCIT," *AIAAPaper92-3943*, 1992.

[17] Goodwin, D. G., Moffat, H. K., and Speth, R. L., "Cantera: An object-oriented software toolkit for chemical kinetics, thermodynamics, and transport processes," 2009.

[18] Browne, S., Ziegler, J., and Shepherd, J., "Numerical solution methods for shock and detonation jump conditions," *GALCIT report FM2006*, Vol. 6, 2008, pp. 90.

[19] Wright, M. J., Candler, G. V., and Prampolini, M., "Data-parallel lower-upper relaxation method for the Navier-Stokes equations," *AIAA journal*, Vol. 34, No. 7, 1996, pp. 1371–1377.

[20] Candler, G., "Hypersonic nozzle analysis using an excluded volume equation of state," *38th AIAA Thermophysics Conference*, 2005, p. 5202.

[21] Johnson, H. B., *Thermochemical interactions in hypersonic boundary layer stability*, University of Minnesota, 2000.

[22] Wagnild, R. M., "High enthalpy effects on two boundary layer disturbances in supersonic and hypersonic flow," Tech. rep., MINNESOTA UNIV MINNEAPOLIS, 2012.

[23] Paquin, L. A., Skinner, S., and Laurence, S. J., "Effect of Wall Cooling on the Stability of a Hypersonic Boundary Layer over a Slender Cone," *AIAA AVIATION 2021 FORUM*, 2021.

[24] Paquin, L. A., Skinner, S., and Laurence, S. J., "Methodology for Investigating the Effects of Wall Cooling on Hypersonic Boundary Layer Transition," *AIAA AVIATION 2020 FORUM*, 2020, p. 2962.

[25] Shumway, N. and Laurence, S. J., "Methods for identifying key features in schlieren images from hypersonic boundary-layer instability experiments," *53rd AIAA Aerospace Sciences Meeting*, 2015, p. 1787.

[26] Pichler, O., Teuner, A., and Hosticka, B. J., "A comparison of texture feature extraction using adaptive Gabor filtering, pyramidal and tree structured wavelet transforms," *Pattern Recognition*, Vol. 29, No. 5, 1996, pp. 733–742.